A UAV-Based Waterway Inspection Method Using Extended Kalman Filter and Multi-band Difference

Zhiling Yu[1], Yingli Li[2], Yansong Duan[1,*]

[1]School of Remote Sensing and Information Engineering, Wuhan University, China - 2025282130135@whu.edu.cn, ysduan@whu.edu.cn
[2]The First Institute of Photogrammetry and Remote Sensing of the Ministry of Natural Resources, China - ylli_fiprs@126.com

Commission II

Keywords: Extended Kalman Filter, Multi-band Difference, Waterway Inspection, Low-overlap Orthophoto, Image Change Detection

Abstract

To address the limitations of traditional manual inspection methods for waterway regulation structures, this paper presents an unmanned aerial vehicle (UAV)-based inspection approach that integrates the Extended Kalman Filter (EKF) and multi-band difference techniques. The EKF is applied to refine low-precision Position and Orientation System (POS) data under very low image overlap conditions. By establishing error state equations and observation models, the EKF dynamically estimates and compensates for systematic and random errors through iterative recursion, enabling the generation of seamless orthophotos. Subsequently, the multi-band difference method is employed on bi-temporal digital orthophoto maps (DOMs). Differential images for each band are generated, weighted, and fused to enhance change features, thereby facilitating the identification of altered regions in waterway structures. Experimental results from the Jiayu section of the Yangtze River demonstrate that the proposed method effectively produces high-quality image mosaics with only 10% image overlap and accurately detects deformations in regulation structures. This approach offers an efficient and automated solution for waterway inspection and monitoring.

1. Introduction

The Yangtze River, as a vital inland waterway with the highest freight volume globally, plays a strategically important role in China's regional development. However, conventional manual inspection methods, such as visual on-foot surveying, are increasingly inadequate to meet the demands of modern waterway management. Unmanned Aerial Vehicle (UAV) aerial photogrammetry has emerged as a promising alternative. Nevertheless, this technique typically requires high image overlap and the placement of ground control points (GCPs), which considerably limits operational efficiency and hinders the goal of high-speed, large-scale inspection. To overcome these limitations, this study proposes a UAV-based waterway inspection method that employs low-overlap flight trajectories and directly integrates UAV Position and Orientation System (POS) data into the photogrammetric process.

Due to cost constraints, POS units installed on drones often exhibit limited accuracy, which hinders seamless orthophoto generation and 3D model reconstruction. Therefore, it is necessary to study the POS refinement of drone images under low overlap and low precision POS conditions, in order to improve POS accuracy and generate seamless orthophotos, providing a data foundation for subsequent 3D reconstruction. The most classic method for POS refinement is the Kalman filter[1], a recursive optimization algorithm used for state estimation and prediction based on system and observation models in continuous time.[2] However, for the specific case of low-overlap UAV images, which have fewer observations and poorer reliability, appropriate improvements to the classic Kalman filter are urgently needed to meet the requirements for precise UAV ground positioning and seamless orthophoto production.

After acquiring multi-temporal data using UAV aerial photogrammetry, comparative analysis of data from different periods is necessary to perform change detection and identify anomalies in waterway regulation structures. The structure and texture of these structures are complex, and data from different periods often contain a wealth of detailed information. For this change detection problem, where detailed differences are significant but overall feature differences are minimal, extracting radiation information from local areas to eliminate detailed information is a question highly worthy of exploration.

In response to the aforementioned issues, we propose a method for UAV waterway inspection utilizing the Extended Kalman Filter and multi-band difference. The contributions of this paper are as follows:

1) An UAV POS refinement method based on the Extended Kalman Filter is proposed. Through iterative recursion, dynamic refinement of POS parameters and effective error compensation are achieved, enabling high-precision direct georeferencing under low-overlap flight conditions.

2) The multi-band difference method is applied to Digital Orthophoto Map data change detection. It involves fusing the resultant difference images to amplify change-related features and applying gradient-based staining analysis to accurately identify and delineate altered regions.

2 Related work

2.1 POS Refinement

In aerial photogrammetric systems, the integrated Position and Orientation System (POS) acquires sensor spatial positions and attitudes via the Global Navigation Satellite System (GNSS) and the Inertial Measurement Unit (IMU). This technology is key to rapid mapping without Ground Control Points (GCPs). However, due to factors such as GNSS errors, IMU drift, time synchronization inaccuracies, and system installation deviations, the raw POS data (often referred to as direct geolocation results) contain systematic errors and cannot meet the requirements for

https://doi.org/10.5194/isprs-archives-XLVIII-2-W12-2026-511-2026

high-precision mapping. Therefore, refining POS data to mitigate or eliminate these errors remains a core research topic in photogrammetry and remote sensing. Current research primarily focuses on tightly-coupled GNSS/IMU integration for continuous relative positioning, multi-source data-assisted refinement, and systematic error compensation.

In the context of tightly-coupled GNSS/IMU integration for continuous relative positioning, Ning et al.[3] proposed a factor graph optimization method based on P-splines to suppress error accumulation. On the other hand, Zhong et al.[4] designed a robust adaptive filtering algorithm to optimize the processing of IMU, GPS, and BDS data, enabling online real-time estimation of measurement noise and thereby improving positioning accuracy.However, such methods suffer from complex error models, and IMU errors are prone to accumulation, leading to a sharp decline in positioning accuracy or even divergence.

In the aspect of multi-source data-assisted refinement, Zhang et al.[5] proposed a visual inertial tight coupling algorithm based on sliding window optimization, which effectively enhanced positioning accuracy. Meanwhile, Lu et al.[6] constructed a mathematical model for the IMU, aligned the poses of monocular vision with the IMU trajectory, and obtained optimal state estimation through sliding window-based nonlinear optimization. However, these methods place high demands on data quality and fusion technology. And the increase in computational load may actually affect real-time performance.

In terms of systematic error compensation, Li et al.[7] proposed a non-iterative algorithm based on linear transformation to calculat the exterior azimuth elements of UAVs directly. Zhang et al.[8] utilized a differential GNSS module combined with the difference algorithm to enhance the accuracy of POS data. Through key technical methods such as position calibration and camera time delay correction, they ultimately obtained high-precision position information at the moment of camera exposure. LaForest et al.[9] analyzed the systematic errors of GNSS/INS-assisted push-broom scanners, thereby performing spatial and temporal calibration. Ponomaryov et al.[10] employed a Kalman filter to optimize differential GPS (DGPS). Gomez-Gil et al.[11] significantly improved positioning accuracy by fusing INS and GPS data using a traditional Kalman filter. Ran et al.[12] proposed a self-calibrating weighted measurement fusion Kalman filter to enhance navigation accuracy.

Although the aforementioned methods can refine POS data to some extent, none have fully resolved the challenge of real-time and efficient optimal attitude estimation for UAVs.

2.2 Image change detection

Image change detection aims to identify changes in land cover and object states by analyzing remote sensing images of the same area acquired at different times. It is widely used in disaster assessment, environmental monitoring, agricultural surveys, and other fields. The core challenges of this technology include radiometric differences, registration errors, interference from seasonal and phenological variations, and the complexity of change categories. Over the past few decades, change detection methods have evolved from pixel-level to object-level approaches.

In the field of pixel-level image change detection, scholars have proposed numerous methods. Johnson et al.[13] applied Change Vector Analysis (CVA) to detect changes by calculating the magnitude and direction of the difference vector between spectral vectors of bi-temporal images. Zhang et al.[14] performed pixel-level change detection based on the ratio method on images, followed by feature change detection on candidate change regions. Wang et al.[15] utilized multi-band image difference method for automated monitoring research on DOM, as this method is more sensitive to discrete object changes.

In the field of object-level image change detection, scholars have also conducted extensive research. Chen et al.[16] systematically elaborated on the theoretical approaches, relative advantages, main issues, and challenges of object-based change detection (OBCD), while also introducing several related algorithms. Grigillo et al.[17] automatically extracted buildings from digital surface models and multispectral orthophotos, performing change detection by comparing rasterized building layers. Liu et al.[18] integrated deep learning techniques with object-based image analysis (OBIA), utilizing convolutional neural networks under the OBIA framework to achieve change feature extraction for image change detection.

Although many scholars have proposed various methods in the field of image change detection, these techniques have not yet been widely applied to the inspection of navigational channel structures.

3 Method

To achieve rapid and efficient automatic inspection of waterways using UAV aerial photogrammetry, this paper proposes a technical process illustrated in Figure 1.

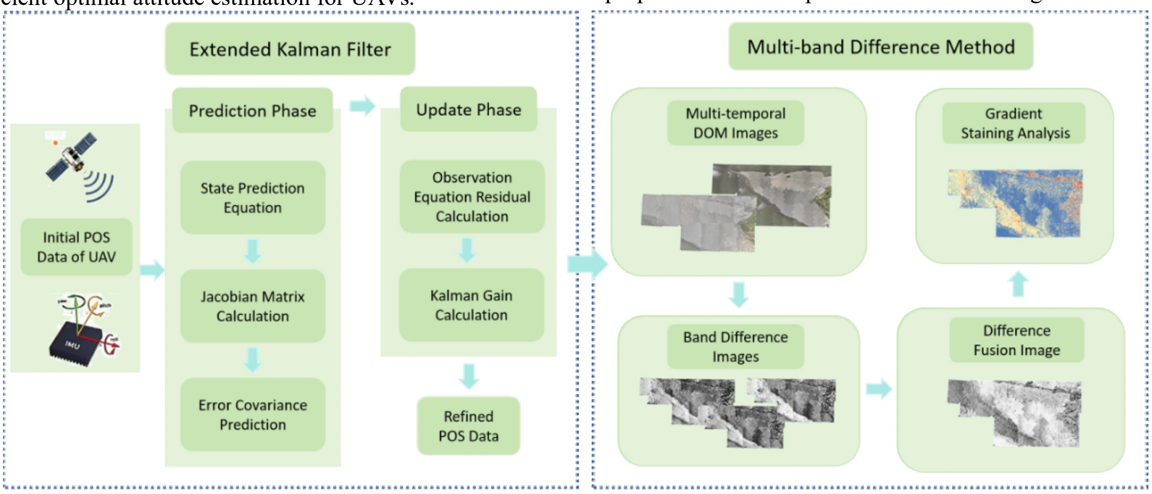

Figure 1. Technical flowchart

Within this framework, we first use UAVs to rapidly acquire aerial images with low POS accuracy and very low overlap rates. The Extended Kalman Filter is then applied to optimize the POS data of the acquired images. The refined POS data are used to generate digital orthophoto maps for two time periods. Finally, change detection is performed using the multi-band difference method to identify altered areas in the waterway regulation structures.

3.1 Extended Kalman Filter

The fundamental principle of the Kalman filter is to use the minimum mean square error as the optimal estimation criterion, combining the previous state estimate and the current observation to compute the current state estimate, thereby achieving local optimality. For nonlinear system models such as those of UAVs, the Extended Kalman Filter (EKF) linearizes the nonlinear mapping relationships in the differential equations. This approach more effectively captures the nonlinear relationships between sensor data and attitude angles, demonstrating improved robustness in dynamic systems.[19]

In discrete time processes, defining the state vector $x \in R_n$ and the measurement vector $z \in R_m$, the state equation and measurement equation can be expressed as:

$$\begin{cases} x_k = f\left(x_{k-1}, k-1\right) + m_{k-1} \\ z_k = h\left(x_k, k\right) + v_k \end{cases} \tag{1}$$

where the nonlinear functions f() and h() represent the mapping relationships between the state vector and measurement vector, corresponding to the sensor models. The terms $m_n \in R_n$ and $v_n \in R_n$ represent mutually independent Gaussian white noise following normal distributions $N(0, Q_k)$ and $N(0, R_k)$, respectively.

After linearizing the nonlinear components in Formulas (1), the result is shown in Formulas (2).

$$\begin{cases} x_k = f\left(x_{k-1}, u_{k-1}, m_{k-1}\right) \\ z_k = h\left(x_k, v_k\right) \end{cases} \tag{2}$$

Taking partial derivatives of f() and h() yields the Jacobian matrices $\Phi\left(k, k-1\right)$ and $H\left(x\left(k\right)\right)$ as Formulas (3).

$$\begin{cases} \Phi\left(k, k-1\right) = \dfrac{\partial f\left(x\left(k-1\right), k-1\right)}{\partial x\left(k-1\right)} \\ H\left(x\left(k\right)\right) = \dfrac{\partial h\left(x\left(k\right), k\right)}{\partial x\left(k\right)} \end{cases} \tag{3}$$

Thus, the state equation and measurement equation can be expressed as Formulas (4).

$$\begin{cases} x\left(k\right) = \Phi\left(k, k-1\right) x\left(k-1\right) + \phi\left(k-1\right) + m\left(k-1\right) \\ z\left(k\right) = H\left(x\left(k\right)\right) x\left(k\right) + y\left(k\right) + v\left(k\right) \end{cases} \tag{4}$$

Defining a new prediction error expression $\tilde{e}_{xk} = x_k - \tilde{x}_k$ and the residual of the measurement vector $\tilde{e}_{zk} = z_k - \tilde{z}_k$. Let $\tilde{x}_k$ be the estimated value of the state vector, and $\tilde{z}_k$ represent the estimated value of the measurement vector. Thus, the expression for the error process can be obtained as shown in Formulas (5).

$$\begin{cases} \tilde{e}_{xk} \equiv A\left(x_{k-1} - \tilde{x}_{k-1}\right) + \varepsilon_k \\ \tilde{e}_{zk} \approx H\tilde{e}_{xk} + \eta_k \end{cases} \tag{5}$$

If $\hat{e}_k$ represents the estimated error, then the posterior state estimate is $\hat{x}_k = \tilde{x}_k + \hat{e}_k$, and the Kalman filter expression for the estimated value $\hat{e}_k = K_k \tilde{e}_{zk}$ is given by the standard update equations. Therefore, the following can be derived:

$$\hat{x}_k = \tilde{x}_k + K_k \tilde{e}_{zk} = \tilde{x}_k + K_k\left(z_k - \tilde{z}_k\right) \tag{6}$$

Thus, based on the fundamental discrete Kalman filter equations, the corresponding time prediction formulas (7) and state update formulas (8) for the Extended Kalman Filter can be derived.

$$\begin{cases} \hat{x}_k^- = f\left(\hat{x}_{k-1}, u_{k-1}, m_{k-1}\right) \\ P_k^- = A_k P_{k-1} A_k^T + W_k Q_{k-1} W_k^T \end{cases} \tag{7}$$

$$\begin{cases} K_k = P_k^- H_k^T \left(H_k P_k^- H_k^T + V_k R_k^- V_k^T\right)^{-1} \\ \hat{x}_k = \hat{x}_k^- + K_k\left(z_k - h\left(\hat{x}_k^-, v_k\right)\right) \\ P_k = \left(I - K_k H_k\right) P_k^- \end{cases} \tag{8}$$

At the initial state, the initial quaternion from the gyroscope sensor during the UAV's static condition and the initial acceleration measurement from the accelerometer sensor are input. The state estimation vector, error covariance matrix, Kalman gain, posterior state estimate, and error covariance matrix are sequentially solved. Through iterative computation, the optimized UAV POS data are ultimately obtained.

3.2 Multi-band Difference Method

To accurately detect changes between two temporal orthophotos, this method identifies alterations in surface features by analyzing radiometric differences between the images. The specific processing steps are as follows:

1) Extract the bands from both images and perform difference operations separately. The calculation formula is:

$$\triangle I_i\left(x, y\right) = I_{2i}\left(x, y\right) - I_{1i}\left(x, y\right) \tag{9}$$

where $I_{2i}\left(x, y\right)$ represents the grayscale value of each band in the later period image, and $I_{1i}(x,y)$ represents the grayscale value of each band in the earlier period image.

2) The difference images are weighted and fused through the following formula to form a unified fused difference image:

$$D_w(x,y)=\sqrt{\sum_{i=1}^{n} w_i\left[\triangle I_i(x,y)\right]^2} \tag{10}$$

where $D_{WL2}(x,y)$ represents the fused difference image, w_i denotes the weighting factors for each band, $\triangle I_i(x,y)$ corresponds to the difference image of each band, and n indicates the total number of spectral bands.

For images with three distinct spectral bands (R, G, B), equal weighting factors are assigned to each band. Thus, the formula adopted in this study for calculating the fused difference image is expressed as:

$$D(x,y)=\sqrt{\sum_{i=1}^{3}\left[\triangle I_i(x,y)\right]^2} \tag{11}$$

3) Finally, gradient-based segmented coloring is applied to the fused difference image based on pixel values, which visually highlights the changed areas. In this representation, deeper red tones indicate more significant changes between the two temporal image datasets.

4 Experiment

To validate the feasibility of the proposed method, we acquired two sets of images of the regulation structures in the Jiayu section of the Yangtze River waterway in June and September 2023 (i.e., before and after the flood season). Image acquisition was conducted using a DJI M3E unmanned aerial vehicle, equipped with a sensor featuring a 24 mm equivalent focal length and a pixel size of 3.3 μm. During image capture, the Position and Orientation System (POS) data, including spatial coordinates and attitude parameters for each exposure moment, were automatically recorded.

The acquired images of the regulation structures in the Jiayu waterway survey area have both flight direction overlap and side overlap of 10%. The two sets of images are shown in Figures 2 and 3, respectively.

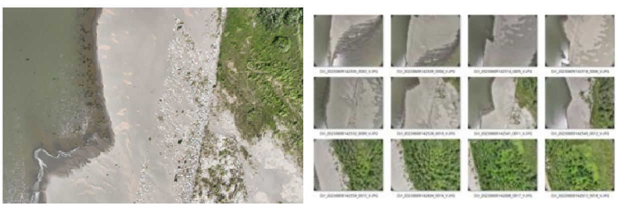

Figure 2. Pre-flood 202306 images (partial)

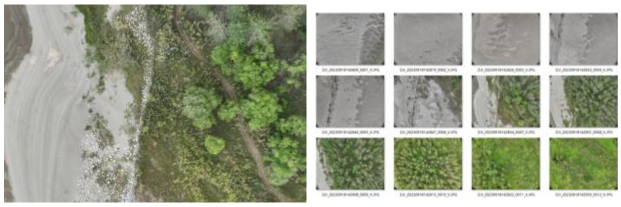

Figure 3. Post-flood 202309 images (partial)

Following the technical workflow proposed in this paper, we first refined the POS data of both temporal image sets using the Extended Kalman Filter. Subsequently, the optimized POS parameters were employed to generate respective Digital Orthophoto Maps. Finally, change detection was performed through multi-band differencing to identify altered regions in the waterway regulation structures, where darker red shades indicate more significant changes between the two temporal datasets.

4.1 POS Refinement Results

To validate the effectiveness of the Extended Kalman Filter refinement method proposed in this paper, we generated two orthophotos using the pre-refinement POS data and the post-refinement POS data respectively from the 202306 data. The processing results are shown in Figure 4.

(a) Original POS orthophoto (b) Refined POS orthophoto

Figure 4. The overall DOM of the 202306 data produced before and after POS refinement

To facilitate a clearer comparison of the processing results, we selected two partial images for display, as shown in Figure 5.

(a) Original splicing details (b) Refined splicing details

Figure 5. Local DOM of 202306 data produced before and after POS refinement

Subsequently, we processed the 202309 data in the same manner, and the obtained results are shown in Figure 6.

(a) Original POS orthophoto (b) Refined POS orthophoto
Figure 6. The overall DOM of the 202309 data produced before and after POS refinement

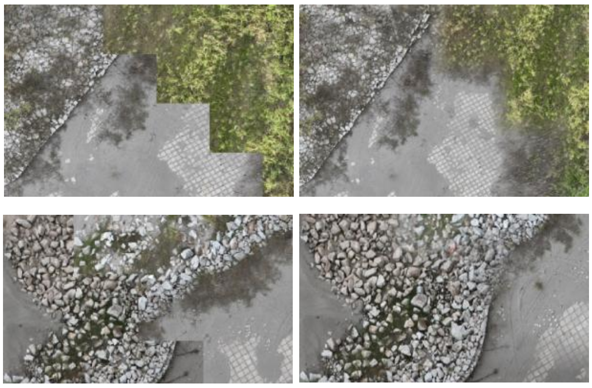

(a) Original splicing details (b) Refined splicing details
Figure 7. Local DOM of 202309 data produced before and after POS refinement

As shown in Figures 5 and 7, the DOM produced using the original POS data exhibits noticeable misalignment, whereas after EKF refinement, the alignment is significantly improved, and misalignments are substantially reduced.

4.2 Change Detection Results

To verify the effectiveness of the change detection method based on multi-band difference proposed in this paper, we processed the two-period DOM using this approach. The result is shown in Figure 8.

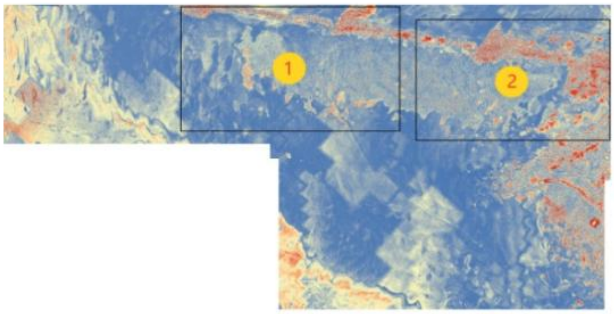

Figure 8. Differential fusion segmented staining image

In Figure 8, deformations in the waterway regulation structures (red areas) are clearly observed. To further illustrate the deformation details, we selected two local areas for analysis, as shown in Figure 9.

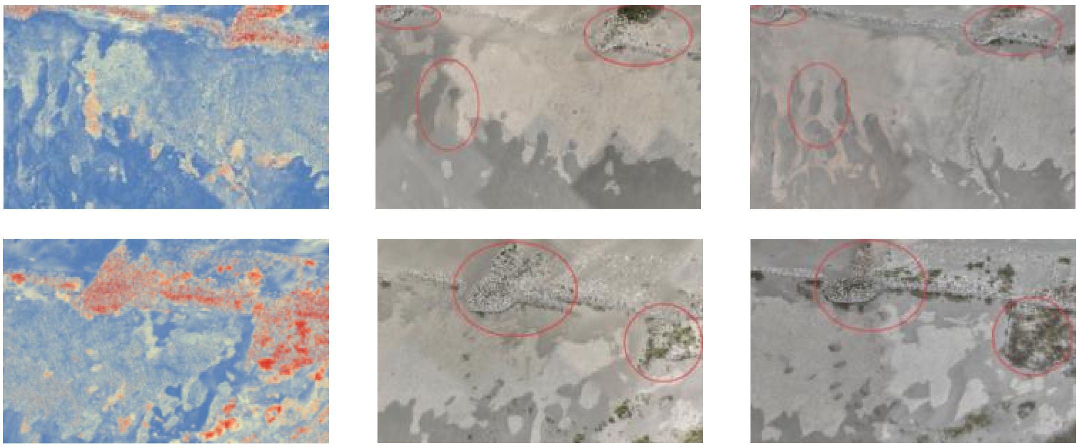

(a) Deformation areas (b) 202306 areas (c) 202309 areas
Figure 9. Schematic diagram of DOM deformation areas

Figure 9 clearly and intuitively demonstrates that due to factors such as water erosion and sediment deposition during the Yangtze River flood season, varying degrees of deformation have occurred in some areas of the waterway regulation structures along the riverbank.

To demonstrate the reliability and universality of this method, we selected orthophoto images from over 50 locations where land cover changes occurred, such as changes in gullies, road construction, and rockfall, for change detection. The results clearly reflected the areas of land cover changes. Some of the detection results are shown in Figure 10.

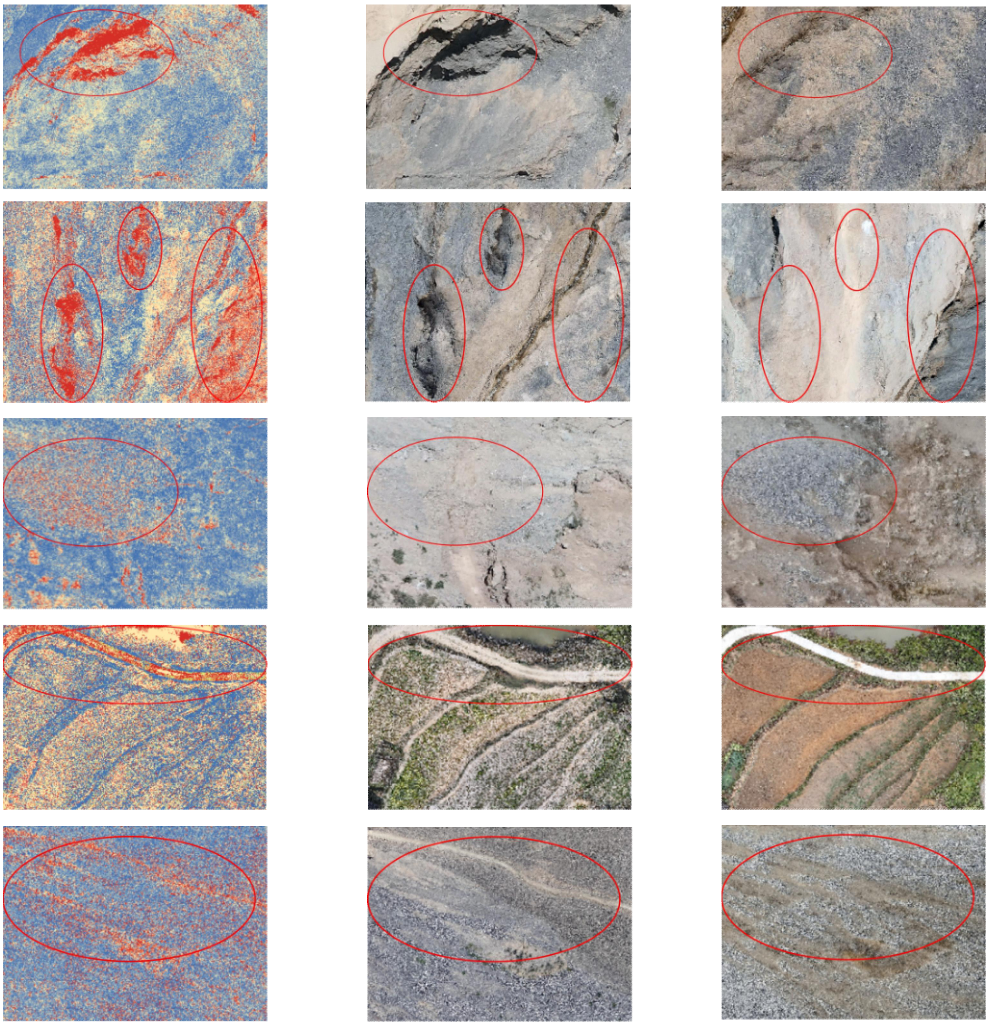

(a) Deformation areas (b) Images before deformation (c) Images after deformation

Figure 10. Schematic diagram of different deformation areas

5 Conclusions and future work

To address the limitations of traditional manual inspection methods for waterway regulation structures, this paper proposes a UAV-based inspection methodology that integrates the Extended Kalman Filter (EKF) and multi-band differencing techniques. The EKF component primarily resolves misalignment issues in UAV image stitching under conditions of low POS accuracy and minimal image overlap. This is achieved by establishing error state equations and observation models for UAV POS data, performing temporal and measurement updates via the EKF, and realizing dynamic parameter refinement and error compensation through iterative recursion. The multi-band differencing technique enables effective change detection between bi-temporal orthophotos by conducting differential processing across spectral bands and fusing the resultant difference images to enhance change-related features, thereby accurately identifying altered regions.

To validate the proposed methodology, two field campaigns were conducted in June and September 2023 (before and after the flood season) along the Jiayu section of the Yangtze River waterway. Experimental results demonstrate that the EKF-based POS refinement method successfully achieves rapid image mosaicking even under challenging weak connection scenarios with only 10% longitudinal and lateral image overlap, producing complete, clear stitched images without gaps or misalignments. The multi-band differencing approach efficiently and precisely detects changed regions in bi-temporal orthophotos, providing an effective solution for deformation monitoring of waterway regulation structures.

The integrated EKF and multi-band differencing methodology presented in this study offers a novel approach for routine inspection and deformation monitoring of Yangtze River waterway structures. This research demonstrates significant potential for practical application and serves as a valuable reference for advancing automation in inland waterway maintenance operations.

References

Kalman, R.E., 1960. A New Approach to Linear Filtering and Prediction Problems. *Journal of Basic Engineering*, 82, 35-45.

Wang, B.W., Sun, Z.B., Jiang, X.Y., et al., 2023. Kalman Filter and Its Application in Data Assimilation. *Atmosphere*, 14(8), 1319.

Ning, B.K., Zhao, F., Luo, H.Y., et al., 2025. Robust GNSS/INS Tightly Coupled Positioning Using Factor Graph Optimization with P-Spline and Dynamic Prediction. *Remote Sensing*, 17(10), 1792.

Zhong, L.N., Chen, H.L., Wang, Z.L., et al., 2022. A Robust Adaptive Filtering Algorithm for the IMU/GPS/BDS Tightly Coupled Integrated Navigation System based on Online Noise Feature Modeling. *34th Chinese Control and Decision Conference (CCDC)*, Hefei, PEOPLES R CHINA, 1392-1397.

Zhang, M., Han, S.S., Liu, X., et al., 2021. Visual-Marker-Inertial Fusion Localization System Using Sliding Window Optimization. *33rd Chinese Control and Decision Conference (CCDC)*, Kunming, PEOPLES R CHINA, 3566-3572.

Lu, J., Xu, Z., 2021. Visual inertial positioning method based on tight coupling. *Gnss World of China*, 46(1), 36-42.

Li, Z., Li, Y., Tang, M., 2014. A Method of Directly Calculating UAV Exterior Azimuth Elements. *Remote Sensing Technology and Application*, 29(3), 506-510+516.

Zhang, K., Yu, G., Gu, G., 2017. The use of differential GNSS to obtain high-precision UAV image line of exterior orientation elements. *Engineering of Surveying and Mapping*, 26(7), 5-11.

Laforest, L.M., Zhou, T., Hasheminasab, S.M., et al., 2021. System Calibration Including Time Delay Estimation for GNSS/INS-Assisted Pushbroom Scanners Onboard UAV Platforms. *Photogrammetric Engineering and Remote Sensing*, 87(10), 705-716.

Ponomaryov, V.I., De Rivera, L.N., Pogrebnyak, O.B., et al., 2000. Increasing of DGPS accuracy by use of Kalman filtering. *Conference on Imaging Technology and Telescopes*, San Diego, Ca, 355-362.

Gomez-Gil, J., Ruiz-Gonzalez, R., Alonso-Garcia, S., et al., 2013. A Kalman Filter Implementation for Precision Improvement in Low-Cost GPS Positioning of Tractors. *Sensors*, 13(11), 15307-15323.

Ran, C.J., Deng, Z.L., 2009. Self-tuning Weighted Measurement Fusion Kalman Filter and its Convergence Analysis. *Joint 48th IEEE Conference on Decision and Control (CDC) / 28th Chinese Control Conference (CCC)*, Shanghai, PEOPLES R CHINA, 1830-1835.

Johnson, R.D., Kasischke, E.S., 1998. Change vector analysis: a technique for the multispectral monitoring of land cover and condition. *International Journal of Remote Sensing*, 19(3), 411-426.

Zhang, Y., Li, L., Jiang, M., et al., 2013. Change Detection Method for Buildings Based on Pixel-level and Feature-level. *Computer Science*, 40(1), 286-293.

Wang, J., Cheng, B., Lu, Z., 2019. Automatic Monitoring of Linear Cultural Heritage Based on Multi-temporal DOM Images. *Geomatics and Information Science of Wuhan University*, 44(1), 77-83.

Chen, G., Hay, G.J., Carvalho, L.M.T., et al., 2012. Object-based change detection. *International Journal of Remote Sensing*, 33(14), 4434-4457.

Grigillo, D., Fras, M.K., Petrovic, D., 2011. Automatic extraction and building change detection from digital surface model and multispectral orthophoto. *Geodetski Vestnik*, 55(1), 28-45.

Liu, T., Yang, L.X., Lunga, D., 2021. Change detection using deep learning approach with object-based image analysis. *Remote Sensing of Environment*, 256.

Jwo, D.J., Cho, T.S., 2010. Critical remarks on the linearised and extended Kalman filters with geodetic navigation examples. *Measurement*, 43(9), 1077-1089.